Whistler waves observed by Solar Orbiter/RPW between 0.5 AU and 1 AU

Matthieu Kretzschmar, T. Chust, V. Krasnoselskikh, D. Graham, L. Colomban, M. Maksimovic, Yu. Khotyaintsev, J. Soucek, K. Steinvall, O. Santolík, et al.

A&A 656, A24 (2021)
https://doi.org/10.1051/0004-6361/202140945

Astronomy & Astrophysics
Special issue

Solar Orbiter First Results (Cruise Phase)

Whistler waves observed by Solar Orbiter/RPW between 0.5 AU and 1 AU

M. Kretzschmar[1], T. Chust[2], V. Krasnoselskikh[1,11], D. Graham[3], L. Colomban[1], M. Maksimovic[4], Yu. V. Khotyaintsev[3], J. Soucek[5], K. Steinvall[3], O. Santolík[5], G. Jannet[1], J.-Y. Brochot[1], O. Le Contel[2], A. Vecchio[4,10], X. Bonnin[4], S. D. Bale[11,12,13], C. Froment[1], A. Larosa[1], M. Bergerard-Timofeeva[1], P. Fergeau[1], E. Lorfevre[6], D. Plettemeier[7], M. Steller[8], Š. Štverák[9], P. Trávníček[11,9], A. Vaivads[3,14], T. S. Horbury[15], H. O'Brien[15], V. Evans[15], V. Angelini[15], C. J. Owen[16], and P. Louarn[17]

[1] LPC2E, UMR7328 CNRS, University of Orléans, 3A avenue de la recherche scientifique, Orléans, France
e-mail: matthieu.kretzschmar@cnrs-orleans.fr
[2] LPP, CNRS, Ecole Polytechnique, Sorbonne Université, Observatoire de Paris, Université Paris-Saclay, Palaiseau, Paris, France
[3] Swedish Institute of Space Physics (IRF), Uppsala, Sweden
[4] LESIA, Observatoire de Paris, Université PSL, CNRS, Sorbonne Université, Université de Paris, Meudon, France
[5] Institute of Atmospheric Physics, Czech Academy of Sciences, Prague, Czech Republic
[6] CNES, 18 Avenue Edouard Belin, 31400 Toulouse, France
[7] Technische Universität Dresden, Würzburger Str. 35, 01187 Dresden, Germany
[8] Space Research Institute, Austrian Academy of Sciences, Graz, Austria
[9] Astronomical Institute of the Czech Academy of Sciences, Prague, Czech Republic
[10] Radboud Radio Lab, Department of Astrophysics, Radboud University, Nijmegen, The Netherlands
[11] Space Sciences Laboratory, University of California, Berkeley, CA, USA
[12] Physics Department, University of California, Berkeley, CA, USA
[13] Stellar Scientific, Berkeley, CA, USA
[14] Department of Space and Plasma Physics, School of Electrical Engineering and Computer Science, Royal Institute of Technology, Stockholm, Sweden
[15] Department of Physics, Imperial College, SW7 2AZ London, UK
[16] Mullard Space Science Laboratory, University College London, Holmbury St. Mary, Dorking, Surrey RH5 6NT, UK
[17] Institut de Recherche en Astrophysique et Planétologie, 9, Avenue du Colonel ROCHE, BP 4346, 31028 Toulouse Cedex 4, France

Received 31 March 2021 / Accepted 7 October 2021

ABSTRACT

Context. Solar wind evolution differs from a simple radial expansion, while wave-particle interactions are assumed to be the major cause for the observed dynamics of the electron distribution function. In particular, whistler waves are thought to inhibit the electron heat flux and ensure the diffusion of the field-aligned energetic electrons (Strahl electrons) to replenish the halo population.
Aims. The goal of our study is to detect and characterize the electromagnetic waves that have the capacity to modify the electron distribution functions, with a special focus on whistler waves.
Methods. We carried out a detailed analysis of the electric and magnetic field fluctuations observed by the Solar Orbiter spacecraft during its first orbit around the Sun, between 0.5 and 1 AU. Using data from the Search Coil Magnetometer and electric antenna, both part of the Radio and Plasma Waves (RPW) instrumental suite, we detected the electromagnetic waves with frequencies above 3 Hz and determined the statistical distribution of their amplitudes, frequencies, polarization, and k-vector as a function of distance. Here, we also discuss the relevant instrumental issues regarding the phase between the electric and magnetic measurements as well as the effective length of the electric antenna.
Results. An overwhelming majority of the observed waves are right-handed circularly polarized in the solar wind frame and identified as outwardly propagating quasi-parallel whistler waves. Their occurrence rate increases by a least a factor of 2 from 1 AU to 0.5 AU. These results are consistent with the regulation of the heat flux by the whistler heat flux instability. Near 0.5 AU, whistler waves are found to be more field-aligned and to have a smaller normalized frequency (f/f_{ce}), larger amplitude, and greater bandwidth than at 1 AU.

Key words. waves – methods: data analysis – solar wind – Sun: heliosphere

1. Introduction

The properties of the solar wind are known to change along its propagation in the interplanetary space. Velocity distribution functions (VDF) of ions and electrons are supposed to be far from equilibrium in the source region of the wind, even under quiet conditions, and the observed dynamics of the different constituents of the wind still raises several questions. Our study is associated with the lightest wind constituent, namely: electrons. It is widely accepted that electrons carry the major part of the heat flux, both in the fast and slow wind, thus their role in the energy balance is very important.
Electron VDF consists of four components. Three are isotropic: the thermal core distribution, the energetic halo distribution in

the energy range from hundreds of eV to several keV, and the even more energetic population, that is, the superhalo, ranging from several keV to several hundreds keV. The fourth population, the so-called strahl, is quite strongly anisotropic and consists of magnetic field-aligned and outwardly propagating energetic electrons in approximately the same energy range as the halo (Rosenbauer et al. 1977; Feldman et al. 1978; Pilipp et al. 1987a,b). It is supposed that the heat flux in the slow and fast wind is carried by different populations of suprathermal electrons. In the slow wind, it is carried by the halo because of its drift velocity shifted in opposite direction in the plasma reference frame, while in the fast wind, it is carried by the Strahl population. Suprathermal electrons are supposed to be created in the tenuous low corona and their evolution is supposed to be weakly collisional or collisionless. This suggests that their dynamics is mainly determined by the wave particle interactions.

In the fast wind, it has been deduced (Maksimovic et al. 2005) from HELIOS measurements that the strahl population significantly decreases between 0.5 AU and 1 AU, while the halo population increases at the same time. Whistler waves are assumed to play an important role in the angular diffusion of the strahl electron, and this is supported by the recent observations of Jagarlamudi et al. (2021) who found an increase of the electrons pitch angle widths in the presence of whistler waves. Parallel whistler waves, however, do not ensure an effective angular diffusion of the strahl electrons and it has been proposed that the diffusion is provided by oblique whistler waves that may be generated when the strahl population has a narrow angular width (e.g., Vasko et al. 2019).

Additionally, the estimates of the heat flux based on measurements of the electron VDF are often found to be significantly smaller than the Spitzer-Härm (Spitzer & Härm 1953) collisional heat flux (Feldman et al. 1976). This implies that wave particle interactions play an important role in the heat flux inhibition. One of the possible mechanisms that may contribute to this is the diffusion of suprathermal halo electrons resulting in the decrease of the halo relative velocity as a result of their interaction with whistler waves. It has been shown by several authors (Gary et al. 1975, 1994; Feldman et al. 1976) that in the slow wind, the heat flux instability can create quasi-parallel whistler waves that may scatter the suprathermal electrons and therefore regulate the heat flux. Such a mechanism is supported by several observations. Using CLUSTER data, Lacombe et al. (2014) found in about 10% of the analyzed spectra the presence of field-aligned, narrow-band, and right-handed circularly polarized waves, which they interpreted as whistlers, finding that their presence was favored by a larger heat flux. Tong et al. (2019a,b) presented observations consistent with the whistler heat flux instability (WHFI) producing quasi-parallel whistlers. However, Vasko et al. (2020) also suggested that the WHFI cannot efficiently regulate the electron heat flux and that its reduction could be attributed to anti-parallel whistlers produced by some other instability (e.g., whistler temperature anisotropy instability; WTAI). It is more difficult to detect these anti-parallel whistlers because they have lower frequencies and often smaller amplitude than parallel whistlers. During the first perihelion of Parker Solar Probe, Agapitov et al. (2020) found the presence of numerous sunward whistlers whose propagation direction relative to the background magnetic field varies from aligned to oblique. Oblique whistlers in their turn can very efficiently diffuse suprathermal electrons (Parail & Pogutse 1978; Vasko et al. 2019). More recently, Halekas et al. (2021) analyzed the heat flux properties observed by Parker Solar Probe near the Sun (0.125–0.25 AU) and found that its regulation is consistent with oblique whistlers and magnetosonic wave modes.

Whistler waves are therefore likely to play an important role in solar wind dynamics, although there is no consensus at present regarding how they are generated under different solar wind conditions and how efficiently they affect the energetic electron population. Solar Orbiter provides us with a great opportunity to explore the role of the whistlers in the solar wind dynamics. Chust et al. (2021) analyzed in detail three wave events observed by Solar Orbiter and found them to correspond to outwardly propagating whistler waves. In this paper, we extend these results by presenting an overview of the waves observed above 3 Hz by the Solar Orbiter RPW experiment between 0.5 AU and 1 AU during its first orbit. We characterize the waves in detail and demonstrate that the wind is populated by quasi-parallel outwardly propagating whistler waves. Then we investigate how the whistler waves properties vary with the heliocentric distance.

Whistler waves at similar distances were observed by the HELIOS spacecraft in the 1970s but in less detail. They were first analyzed by Beinroth & Neubauer (1981) and more recently by Jagarlamudi et al. (2020). The authors used the data obtained by only two components of the search coil magnetometer, which limited their analysis of the dependence of amplitudes upon different parameters. Some of our results show some disagreement with these previous studies. It is worth recalling that there were other statistical studies of whistler waves in the solar wind at 1 AU, in particular using CLUSTER (Lacombe et al. 2014) and ARTEMIS (Tong et al. 2019a) spacecraft measurements. To the exception of Lacombe et al. (2014) at 1 AU, none of these statistical analyses could make a complete polarization analysis to experimentally demonstrate that the observed waves actually correspond to whistlers waves. Here, we compare our results with these previous studies when possible.

The paper is organized as follows. Section 2 presents the data and the wave detection method. In Sect. 3, we determine the wave polarization and propagation direction, discussing the method and instrumental issues in detail. Section 4 presents the variations of the wave properties with the heliocentric distance and we present our conclusions in Sect. 5

2. Data and analysis

Our analysis is based on measurements carried out between March 1, 2020 and December 3, 2020, using the magnetic and electric antennas (respectively SCM -Search Coil Magnetometer- (Jannet et al. 2021) – and ANT) of the Radio and Plasma Waves (RPW, Maksimovic et al. 2020) experiment on board Solar Orbiter. The data cover slightly more than the first orbit, at distances between 0.51 and 0.98 AU from the Sun. Snapshot waveforms of the fluctuating magnetic field and electric antenna voltage differences are regularly recorded at 256 Hz, 4 kHz and 25 kHz by the Low Frequency Receiver (LFR). With the three electric antenna being in the same plane, we can only access components of the electric field in that plane. Therefore, here we use the spacecraft reference frame (SRF) that is most often closely related to the RTN frame ($X \sim -R$, $Y \sim -T$, $Z \sim N$). As explained in Maksimovic et al. (2020), computing the E_z component requires the combination of two different measurements, which makes this quantity less reliable at this early stage of the mission. We therefore focus on the E_y component that is determined as follows: $E_y = -V_{23}/L_y$, where L_y is the effective length which will be discussed later. A few solar wind signals were recorded by SCM above 128 Hz and we considered

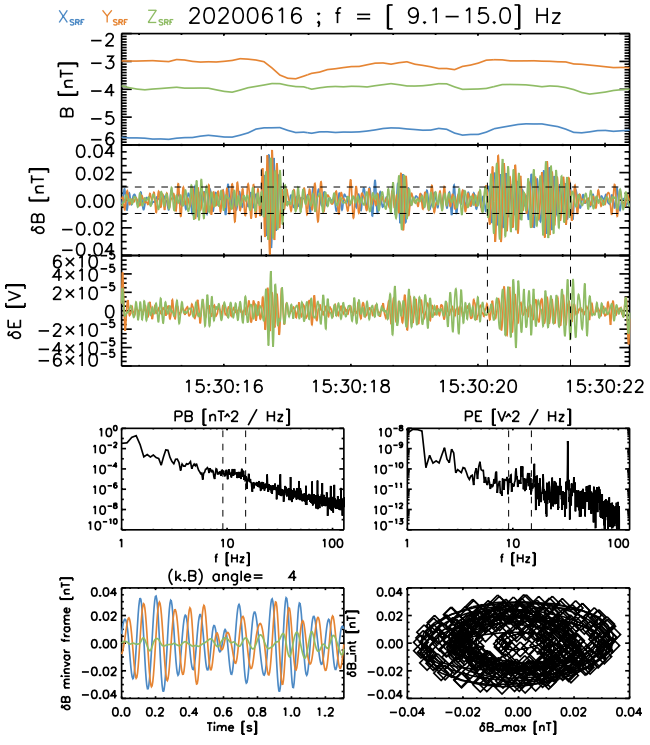

Fig. 1. Example of RPW/LFR snapshot at 256 Hz and wave packet detection. *Three first rows* show the background magnetic field, and the AC magnetic (X, Y, and Z components), and electric field (Y and Z components). Horizontal dashed lines shows three times the noise level and vertical dashed lines indicate the detected wave packets. *Fourth row* shows the magnetic and electric power spectra. *Fifth row* show the minimum variance analysis and hodogram for the longest wavepacket, indicated in the AC electric field panel (third row).

only the snapshot acquired with a sampling frequency of 256 Hz, each of them having a duration of 8 s.

At this early stage of the mission, there are two uncertainties in the RPW measurements that we had to deal with: the first one was pointed out and discussed in detail by Chust et al. (2021) and it concerns a systematic, non-frequency-dependent, phase shift (also called phase deviation in the following) between the magnetic and electric measurements. However, because for electromagnetic waves aligned with the background magnetic field, as the ones that we are going to describe, δE and δB must be perpendicular, this observed phase shift can be identified and corrected, although its origin is still unclear for now. The second uncertainty is the effective length L_y of the electric antenna, which appears to be a difficult quantity to characterize in the interplanetary medium, as reported by Mozer et al. (2020) on Parker Solar Probe. Steinvall et al. (2021) estimated it for Solar Orbiter by performing a deHoffmann-Teller analysis and comparing velocity measured by the Proton-Alfa Sensor (PAS) of the Solar Wind Analyser (Owen et al. 2020, SWA). We find similar values of L_y by comparing the theoretical and observed phase velocity of whistler waves, as presented in Sect. 3.3, which will allows us to identify the anti-sunward propagation of these waves.

We also used the following data, when available: the electron density from RPW (Khotyaintsev et al. 2021), the measurements of the Solar Orbiter DC magnetometer MAG (Horbury et al. 2020) –which allows us to retrieve the direction of the background magnetic– field and the measurements of the solar wind moments acquired by the Solar Wind Analyser (SWA) instrument (Owen et al. 2020).

Our objective is to automatically detect the waves and compute their parameters. We have chosen a conservative approach that allows for false detections, which we removed afterwards by applying various additional criteria. We analyzed a snapshot if its 8 s average spectrum was at least three times larger than the background spectrum in a frequency band of at least 1 Hz. The background spectrum was determined as the daily median spectrum, which gave good results as intervals containing waves occupy only a small fraction of the observations. A similar level of detection was obtained by using a threshold on the coherence between the magnetic components. For each 8 s snapshot with waves, we performed a standard analysis by computing the average magnetic spectral matrix (df = 2 Hz) and determining the frequency band and maximum frequency of the waves, as well as the **k** vector direction (with a $\pm\pi$ ambiguity but **k** was initially forced to be in the same half plane as the background magnetic field, $\mathbf{B_0}$). We also evaluated the degree of polarization and the ellipticity of the waves. This was done in two ways: by computing them directly from the observed spectral matrices, as suggested by Means (1972), and by doing a singular value decomposition analysis of this same matrix, as proposed by Santolík et al. (2003). The results from the two methods agree very well with each other and the choice of one or another does not make differences for the statistical results presented here. For each snapshot, we kept the values of the wave parameters obtained at the frequency corresponding to maximum of the normalized spectrum.

To gain deeper insights into the observed waves, we added a procedure for detecting individual wave packets within a snapshot. We first pass-band filtered the magnetic and electric waveforms in the frequency band determined by analyzing the 8 s averaged spectrum. Next, we selected periods where the magnetic field root mean square (rms) was found to be three times higher than the noise level for at least four periods, which defines a wave packet. Wave packets separated by less than 1.5 periods were merged. Figure 1 shows as an example a snapshot observed on June 16, 2020, near 15:30. Two wave packets were detected on that snapshot, while the shorter wave packet around 15:30:19 does not remain for enough time above our threshold to be detected. The properties of individual wave packet were determined both via a Fourier analysis to retrieve the wave amplitudes and phases as well as via a minimum variance analysis (MVA, Sonnerup & Scheible 1998) of the magnetic waveforms to retrieve the direction of the wave vector ($\pm\pi$). We also estimated their planarity and ellipticity by using the ratio of the singular values (Santolík et al. 2003). In comparison to the 8 s average spectral matrix, we can perform a single (non averaged) Fourier transform as the analysis is limited to the time where the wave signal is significant and, thus, the incoherent noise to be averaged is less relevant.

The quality of the wave parameters deduced from individual wave packet depends on their duration and signal to noise ratio (S/N), meaning that we observed a greater dispersion among the values for shorter wave packets. One advantage of analyzing individual wave packets resides in the possibility to better determine the temporal filling factor of the waves; we also aimed at performing a more precise analysis of faint wave packets whose signal in the spectrum would be relatively weak.

The detection methods described above sometimes commit errors that may be caused by some spacecraft or instrumental interferences. We used additional criteria to remove some obvious erroneous detections, caused by signals from the platform or instrumental problems, as well as "waves" with a planarity or

ellipticity (as deduced from the average spectral matrices) less than 0.6, or with a phase shift between the maximum and intermediate components in the wave frame that stray from |90|° by more than 10°. By doing so, we focused on circularly polarized waves but the inspection of the events with low value of planarity or ellipticity points preferably towards instrumental interferences rather than actual solar wind signals, although this later explanation cannot be ruled out at this stage. Due to the presence of interferences and the low sensibility of SCM at low frequencies, we considered only frequencies above 3 Hz and, finally, we kept only the events for which we dispose measurements of the DC magnetic field.

We ended up with 5035 spectra computed over 8 s and 17362 associated wave packets, most of which have a right-handed circular polarisation and are quasi-aligned with the magnetic field, as described in the next section.

3. Wave polarization and propagation direction

In this section, we analyze in detail the wave properties, first in the spacecraft frame and then in the plasma frame, in order to identify the wave modes as unambiguously as possible. The top panel of Fig. 2 shows the spectrogram of the detected events in chronological order, but with a non linear time scale. The distance of the Sun at which they were observed is indicated as well. We can note the traces of interferences and artefact signals as horizontal straight lines. There are almost no waves observed in the frequency range above approximately 90 Hz and an overwhelming majority lie in the frequency range from 0.04 to $0.3 f_{ce}$, with a maximum around $0.1 f_{ce}$ (f_{ce} is the electron gyrofrequency) in the spacecraft reference frame. The group of waves with frequencies clearly above $0.1 f_{ce}$ that occurred at the beginning of the orbit around 0.85 AU corresponds to a strong magnetic perturbation (possibly a magnetic cloud or ICME) that crossed Solar Orbiter on April 13, 2020. We often treat the waves registered during this perturbation separately and focus on waves observed during less perturbed time intervals.

The middle panel shows the power spectral density of the magnetic field for each wave packet. As can be seen from the color code, most of the waves are quasi-aligned with the background magnetic field. A few of them have a significant deviations from parallel propagation: 1.5% have an angle greater than 40° and 0.9% have an angle greater than 60°. It is noticeable that these waves also have a lower amplitude of the magnetic field, as expected for oblique whistler mode waves.

The polarization of the wave packets in the spacecraft frame is shown in the bottom panel of Fig. 2. As we noted already, most of the waves are aligned with the background magnetic field, therefore, $\theta_{\mathbf{k},\mathbf{r}} \sim \theta_{\mathbf{B_0},\mathbf{r}}$, and the abscissa also indicates approximately the angle between the background magnetic field and the radial direction. When the background magnetic field, $\mathbf{B_0}$, points in the direction of the Sun (small angles), the phase difference between B_y and B_z is positive and close to 90°; whereas when B_0 points outward, the phase difference is negative. The overwhelming majority of these waves are right-handed (RH) in the spacecraft frame. Evaluation of the phase difference between the largest and middle eigenvectors in the MVA frame (not shown here), with the k-vector and background magnetic field vector assumed to be in the same half-space with respect to the plane formed by these eigenvectors, confirming that the waves are RH ($\sim +90° \pm 10°$). Only 0.6% of the events (109 packets) have left-hand (LH) polarization in the spacecraft frame, but these are also the waves that were found to be more oblique: 73% of them have a ($\mathbf{k}$,$\mathbf{B_0}$) angle above 50°. By contrast, only 0.7% of the RH polarized waves have a ($\mathbf{k}$, $\mathbf{B_0}$) angle above 50°. We leave these interesting but non-typical events for future studies and we concentrate here on relatively field-aligned ($\theta_{\mathbf{k},\mathbf{B_0}} < 40°$) and RH polarized waves, which are sound candidates for being whistler waves.

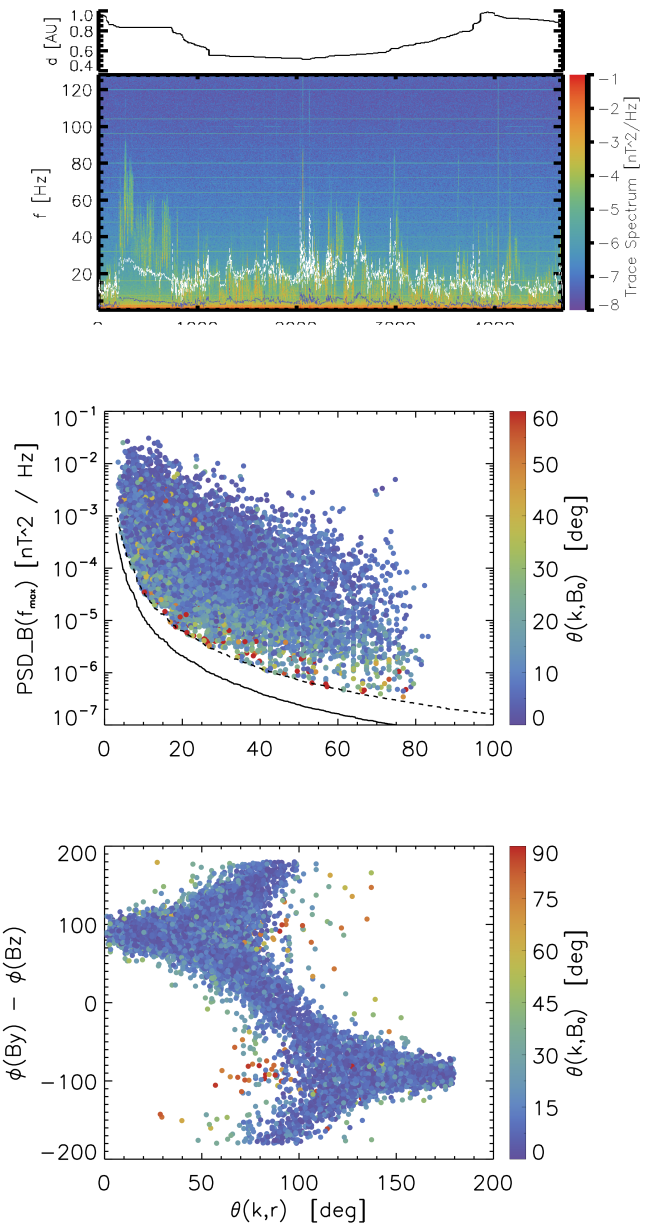

Fig. 2. Overview of the detected waves. *Top*: 8 s average trace spectrum for the detected events versus the event number, with their distance from the Sun on the top. Dashed white line indicate $0.1 f_{ce}$ and the violet one the lower hybrid frequency, f_{LH}. *Middle*: magnetic field PSD at the frequency corresponding to the maximal power for each detected wave packet. The noise level is indicated by the plain black line, and three times the noise by the dashed line. The color indicates the angle between the **k** angle and the background magnetic field. *Bottom*: phase shift between the B_y and B_z magnetic components versus the angle between the **k** vector and the radial direction. The color indicates the angle between the **k** angle and the background magnetic field.

Their observed frequencies and RH polarization do indeed correspond to the frequency range and polarization of whistler waves. However, these observed properties are Doppler-shifted by the solar wind velocity and the actual identification of the waves requires to determine them in the plasma reference frame.

As we encountered two instrumental difficulties, which is not surprising at this stage of the mission, the phase deviation between E and B and the value of the effective length of the electric antenna, we think it is important to fully describe how we tackled them. We give a brief outline of the method here before describing it in detail in the subsequent sections. We first inspected the phase difference between E_y and B_z to investigate whether the quasi-parallel waves propagate sunward (equivalently inward) or anti-sunward (equivalently outward). This leads us to two possible scenario for the phase deviation corresponding to the two propagation directions, which will be resolved by comparing the effective lengths. For both scenarios, we determined the wave frequency and theoretical phase velocity in the plasma frame by applying the Doppler shift and using the plasma dispersion relation for whistler mode waves. Then, we compared the observed and theoretical wave phase velocities to determine the effective length in both scenario. Finally, we found the anti-sunward scenario to be the only one that provides realistic effective lengths that are in excellent agreement with an independent analysis using the deHoffman-Teller frame.

In anticipation, we note that our corrections of the E and B phase deviation and our derived relation for the effective length antenna – which lead us to the conclusions that the observed waves are anti-sunward propagating whistler waves – are respectively consistent with the studies of Chust et al. (2021) and Steinvall et al. (2021), and appear therefore reliable.

3.1. Doppler shift

Determining the wave properties in the plasma reference frame requires us to perform the Lorentz transformation of the fields, which results from the wave being convected by the solar wind as seen from the spacecraft. If the waves propagate outward, the frequency in the plasma reference frame increases and the polarization remains unchanged with respect to the observations in the spacecraft reference frame. On the other hand, if the waves propagate inward, the frequency decreases and the polarization may also change if the phase velocity of the wave is smaller than the solar wind speed. Taking into account the observed frequency and polarization in the spacecraft frame, the observed RH waves can be 1) outwardly propagating whistler waves, 2) inwardly propagating whistler waves with $v_\varphi > v_{SW}$ (the waves are therefore inwardly propagating in the spacecraft frame), or 3) inwardly propagating ion cyclotron waves with $v_\varphi < v_{sw}$ (the waves are therefore outwardly propagating in the spacecraft frame.) Here, v_φ stands for the phase velocity of wave. The phase speed of ion cyclotron waves (ICW) is close to the Alfvén velocity V_A. In our sample, assuming $n_p = n_e$ and using the electron density from the spacecraft potential, V_A has a median value of $36\,\mathrm{km\,s^{-1}}$ and a standard deviation of $17\,\mathrm{km\,s^{-1}}$. It is therefore always well below the solar wind speed and the inward ICW could be observed with a RH polarization in the spacecraft frame with an outward velocity of $v_{sw} - V_A \sim 0.9 v_{sw}$, namely, close to the solar wind speed. Inward whistler mode waves should be observed with an inward velocity of $v_\varphi - v_{sw}$ and outward whistler mode waves with an outward velocity of $v_\varphi + v_{sw}$.

Therefore, even with an ambiguity in the determination of the wave propagation direction caused by the uncertain phase difference between E and B (the "phase deviation" problem), the analysis of the absolute phase speed velocity and its comparison to theoretical expectations can provide us with a strong argument in favor of one of the two options proposed above.

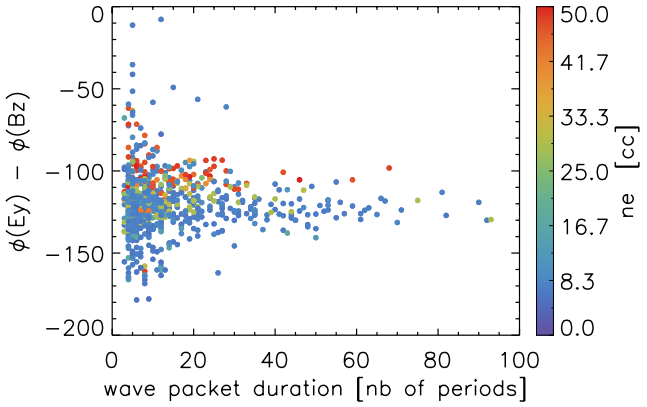

Fig. 3. Phase difference between E_y and B_z versus the wave packet duration and electron density deduced from the spacecraft potential.

3.2. Direction of wave propagation

The wave propagation in the plasma frame is the direction of the Poynting flux; it can be determined by conjointly using the magnetic and electric fields measurements. The RPW can only determine the Y and Z components of the electric fields E_y and E_z, which are in a plane perpendicular to the X direction which is most often the radial direction. At this stage of the mission, the Y component is the most reliable as it is determined directly from the voltage difference between two symmetric antennas, the evaluation of the Z component requiring a combination of measurements coming from the three antennas. As we are dealing with plane waves aligned with the background magnetic field, we stress that only one component of the electric field is necessary to remove the $\pm\pi$ ambiguity on the waves propagation direction determined with the magnetic field. As indicated previously, $E_y = -V_{23}/L_y$. The value of L_y can depend on plasma conditions and is known to be difficult to assess; it affects the absolute value of the electric field estimate but not its phase. Here, we first discuss the propagation direction of the wave.

The projection of the Poynting vector of the waves in the X direction depends on the product of $E_y.B_z$ and therefore on the phase difference between E_y and B_z. For a plane wave parallel to the background magnetic field, which is itself aligned with the radial direction (±X), the phase difference between E_y and B_z must be either 0° if the wave propagates towards the Sun ($\boldsymbol{E_y} \times \boldsymbol{B_z}$ in the $+X$ direction), or 180° if the wave propagates outward. Figure 3 shows the phase difference of $\varphi_{E_y} - \varphi_{B_z}$ for right-hand circular polarized waves that propagates parallel (or anti-parallel) both to the background magnetic field B_0 ($\theta_{\mathbf{k},\pm\mathbf{B_0}} < 20°$) and to the radial direction ($\theta_{\mathbf{k},\pm\mathbf{X}} < 20°$). It is plotted as a function of the wave packet duration that we use as a criterion for the signal to noise ratio. The color indicates the electron density. We can see that the phase difference is nearly constant and approximately equal to −130°; it does not appear to vary with the frequency (not shown), indicating a propagation in the half plane anti sunward to the Sun. The first conclusion is therefore that all these waves propagate in the same direction. We also note a tendency for the phase difference to slightly increase for larger densities, the reason for this being unclear at this point. However, this value of −130° does not match the wave vector direction found with the magnetic field, for which we should find either −180° or 0°. Our interpretation of this unexpected phase deviation, similar to that deduced by Chust et al. (2021) based on the detailed analysis of a few single whistler events, is that this is caused by an unsolved instrumental problem.

Since the phase deviation is well established for the parallel (or anti parallel) whistler waves, our conclusion is that there is a constant error in the registration of the phase of one of the two signals, which leaves us with two possible scenario: 1) a "weak phase deviation" for which E_y (resp., B_z) should be delayed (resp., advanced) by removing (resp., adding) 50°, so that the phase difference matches 180°. This will lead to the conclusion that the waves propagate outward; and 2) a "strong phase deviation" for which E_y (resp., B_z) should be advanced (resp., delayed) by adding (resp., removing) 130°, so that the phase difference matches 0°. Such a phase difference will correspond to waves that propagate inward. The same conclusion can be drawn by analyzing the phase difference between E_y and B_y, which has to be equal to ±90°. We present below some extra argument that indicates that the first option is very likely to be correct. In any case, it is important to notice that the (B_z, E_y) phase difference remains constant for practically all the parallel waves and frequencies, which provides a strong argument in favor of the notion that the large majority of waves observed between 1 AU to 0.5 AU are propagating in the same direction.

3.2.1. Wave frequency in the plasma frame

The observed frequency in the spacecraft frame (superscript $^{\rm SC}$, quantities in the solar wind frame have no superscript) $\omega^{\rm SC}$ has been Doppler shifted by the motion of the solar wind so that:

$$\omega = \omega^{\rm SC} - \boldsymbol{k}.\boldsymbol{V_{\rm SW}} \tag{1}$$

Or, supposing that both k and $V_{\rm SW}$ are positive quantities,

$$\omega_{\rm in,out} = \omega^{\rm SC} \pm kV_{\rm SW}|\cos\theta_{\boldsymbol{k},\boldsymbol{V_{\rm SW}}}|, \tag{2}$$

where the subscripts $_{\rm in}$ and $_{\rm out}$ stand for inward (sign +) and outward (sign −) propagation, respectively. Combining this equation with the following plasma dispersion relation for whistler mode waves in a cold plasma approximation,

$$k = \frac{\omega_{\rm p}}{c}\sqrt{\frac{\omega}{\Omega_{\rm c}\cos\theta - \omega}}, \tag{3}$$

we can derive the frequency in the plasma frame:

$$\omega_{\rm in,out} = \omega^{\rm SC} \pm V_{\rm SW}|\cos\theta_{\boldsymbol{k},\boldsymbol{V_{\rm SW}}}|\frac{\omega_{\rm p}}{c}\sqrt{\frac{\omega_{\rm in,out}}{\Omega_{\rm c}\cos\theta - \omega_{\rm in,out}}}, \tag{4}$$

where ± corresponds to inward and outward propagation, respectively. We solved this expression numerically using Brent's method (Brent 1973). We used the electron density determined by RPW from the spacecraft potential measurements and the solar wind velocity measured by SWA whenever available, which is rare (SWA has unfortunately not been working continuously): in most of the cases, we had to assume a purely radial solar wind speed of 350 km s^{-1}. The validity of this assumption will be discussed later. Once the frequency in the plasma frame determined, we can compute the theoretical wave vector and phase velocity, $v_\varphi = \frac{\omega}{k}$, in the two scenarios.

3.2.2. Phase velocity in the plasma frame

The observed phase velocity $v_\varphi = \omega/k$ can be computed by considering the Faraday equation for waves,

$$\mathbf{k}\times\mathbf{E} = \omega\mathbf{B}, \tag{5}$$

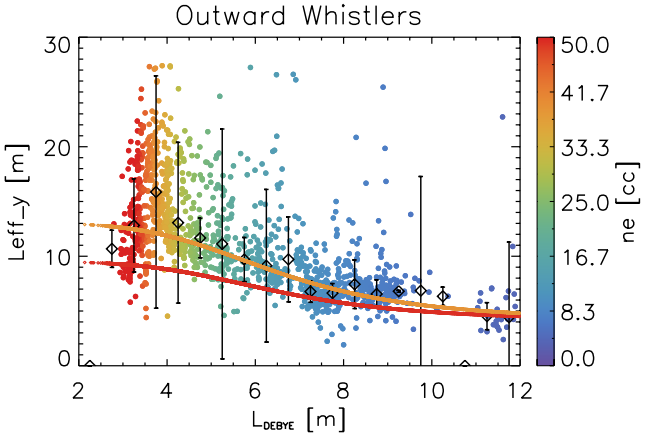

Fig. 4. Effective length considering outwardly propagating whistlers. The relation obtained by Steinvall et al. (2021) using deHoffmann-Teller analysis is in red, the modified one ($L_{\rm eff}$, max = 13 m) in orange.

which easily leads to the following expression (Chust et al. 2021):

$$\hat{v}_\varphi = \frac{\mathbf{n}.\mathbf{B_0}(\hat{E}_y\hat{B}_y^*)}{B_{0x}(\hat{B}_z\hat{B}_y^*) - B_{0z}(\hat{B}_x\hat{B}_y^*)}, \tag{6}$$

where $\mathbf{n} = \frac{\mathbf{k}}{k}$, $\mathbf{B_0}$ is the background magnetic field, $\hat{}$ denotes the complex amplitude and * the complex conjugate.
The equation is valid for a plane wave when there is no parallel fluctuating electric field, which is our case here. It allows us to consider non purely radial propagation, but gives the same results $\hat{v}_{\rm ph} = \hat{E}_y/\hat{B}_z$ in this latter case. The multiplier $\hat{B}_y^*$ could be removed but it allows us to work with relative phases more easily; the cross terms, $\hat{B}_i\hat{B}_j^*$ or $\hat{E}_i\hat{B}_j^*$, are averaged when computed from the averaged spectral matrix obtained from the 8 s snapshot.

Furthermore, v_φ, as expressed in Eq. (6) is in the solar wind frame if we use the electric field in the solar wind frame. The latter can be determined by considering that the solar wind frame is moving with $v_{\rm sw}$ in the $-X_{\rm SRF}$ direction, as seen from the S/C frame and applying the classical Lorentz transformation and :

$$\mathbf{E} = \mathbf{E}^{\rm sc} + \mathbf{v}\times\mathbf{B}, \tag{7}$$

where $\mathbf{E}^{\rm sc}$ is the electric field measured in the spacecraft frame. For E_y, using complex notation for the fluctuating field, $E_y = \Re(\hat{E}_y e^{ikr-i\omega t})$, this leads to:

$$\hat{E}_y = \hat{E}_y^{\rm sc} - v_x\hat{B}_z = \hat{E}_y^{\rm sc} + v_{\rm sw}\hat{B}_z \tag{8}$$

where we have assumed that the wind flows in the radial direction only.

Equivalently, one can compute the phase velocity in the spacecraft frame by using Eq. (6) with $E_y = E_y^{\rm sc}$ and then remove $\boldsymbol{k}.\boldsymbol{V_{\rm SW}}/k$ from the result.

Let us emphasize that the observed wave phase velocity is anti correlated with the effective length $\hat{E}_y^{\rm sc} = \frac{\hat{V}_y^{\rm sc}}{L_{\rm eff}}$, where $\hat{V}_y^{\rm sc}$ is the fluctuating electric potential observed in the spacecraft frame in the Y direction.

3.3. Effective length of electric antenna

At this stage of the mission, the effective length of the antenna is not yet unambiguously known. Its value is important as it

affects the evaluation of the amplitude of the electric field and therefore the estimate of the wave velocity. We can estimate the effective length by comparing the measured phase velocity in the solar wind frame and the expected velocities obtained from the dispersion relation (Eq. (3)). The measured velocity is obtained by using Eq. (6) with the electric field in the solar wind frame (Eq. (8)) and by taking into account the corrections discussed above for the phase deviation The relation $v_\varphi = \frac{\omega}{k}$ leads to the following equation for the effective length estimate:

$$L_{\rm eff} = |\frac{\hat{V}_y^{\rm sc}\hat{B}_y^*}{\frac{\omega}{k}\frac{B_{0x}(\hat{B}_z\hat{B}_y^*)-B_{0z}(\hat{B}_x\hat{B}_y^*)}{\mathbf{n}.\mathbf{B_0}} - V_{\rm sw}\hat{B}_z\hat{B}_y^*}|. \quad (9)$$

This equation can be separately applied to inwardly ($\varphi_{\rm corr} = 130°$ and $\frac{\omega}{k} = \frac{\omega_{\rm in}}{k_{\rm in}}$) and outwardly ($\varphi_{\rm corr} = -50°$ and $\frac{\omega}{k} = \frac{\omega_{\rm out}}{k_{\rm out}}$) propagating whistler mode waves. The measured effective lengths, derived for outwardly propagating whistlers propagating at less than 60° from the radial direction (to avoid low E_y value) and computed from the 8s averaged spectra are shown in Fig. 4. There is a very good agreement with a different and independent estimate of the effective length, represented in red and obtained by Steinvall et al. (2021); this latter was derived by matching the velocity of the deHoffmann-Teller (HT) frame, deduced from RPW measurements of the DC electric and magnetic fields, to the measurements of the solar wind velocity by SWA/PAS. The curve in orange is a variation of the Steinvall et al. equation, by taking $L_{\rm eff,max} = 13$ m instead of 9.5 m in their Eq. (3): $L_{\rm eff} = L_{\rm eff,min} + \frac{L_{\rm eff,max}-L_{\rm eff,min}}{1+(\lambda_d/L_{\rm antenna})^4}$, where λ_d is the Debye length. Assuming inwardly propagating whistler waves leads to much longer nonphysical effective lengths, in clear disagreement with the deHoffmann-Teller analysis. This can be understood since in this case the phase velocities in the spacecraft frame would be significantly smaller (only inward whistlers with phase velocities faster than the wind speed keep the RH polarization in the spacecraft frame), which would therefore require a larger $L_{\rm eff}$ (smaller E_y) to match the expected phase speed, $\frac{\omega}{k}$. There is still a significant dispersion of the points in our estimate of the effective length, and additional work and more statistics are required to obtain a definitive value that can be used as a standard for the calibration of the electric field. This will be done in future studies.

Nevertheless, the very good agreement between the evaluations by two independent methods of the effective length of the antenna provides an additional argument in favor of the weak phase deviation corresponding to outwardly propagating whistler waves. Furthermore, since we can now better cross-calibrate the electric and magnetic field by applying the phase correction (−50°) and having a reliable estimate of the effective length, we can get a more reliable estimate of the phase speed.

3.4. Wave velocity and mode identification

The phase velocities evaluated in the solar wind reference frame, obtained by making use of the electric and magnetic fields measurements and taking into account the modified Steinvall et al. relation for the effective length ($L_{\rm eff,max}$ = 13m instead of 9.5m), are presented in Fig. 5 for the same set of the events as presented in Fig. 4. The observed values vary in the range from less than 100 km s^{-1} to more than 1000 km s^{-1}, and can thus be both larger or smaller than the velocity of the solar wind. The velocity obtained using the relation dispersion for three cases are plotted for reference; the agreement with the theoretical expectations obtained by using the observed value of $f_{\rm ce}$ and $f_{\rm pe}$ for each single point, not shown for clarity, is excellent – namely, below $n_{\rm e} \sim 30$ cm^{-3}.

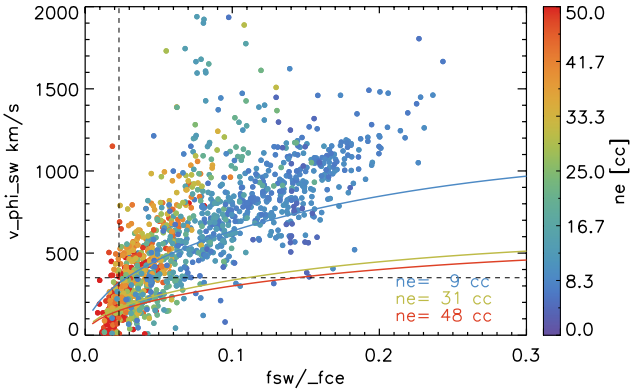

Fig. 5. Phase velocity in the solar wind frame. Theoretical velocities for quasi-aligned whistler with $f_{\rm ce} \sim 190$ Hz and different value of electron density are shown for reference as plain colored lines. The vertical dashed lines indicates the lower hybrid frequency, the horizontal dashed line indicates the typical solar wind velocity.

At densities above ~30 cm^{-3} corresponding to Debye length of ~4m, as could be anticipated from Fig. 4, the observed velocities are often larger than expected. To investigate whether this compromise the identification of the waves as whistler mode, we show in Figs. 6–9 the detailed analysis for four representative cases for which plasma parameters were available. For each figure, the three first panels show the context of the wave observation, the two next panels show the magnetic and electric filtered waveforms, and the three last panels show the coherence and phase difference, as well as the observed and theoretical wave phase velocity. The phase difference are plotted without and with (in dashed line) the correction of −50° for the electric field. The observed wave phase velocity is computed using the effective length relation derived in the previous section (orange curve on Fig. 4).

The two first examples in Figs. 6 and 7 show cases at low and intermediate density for which the agreement between the expected and observed phase velocity for outwardly propagating whistler is very good. The correction for the phase deviation allows us to retrieve the expected behavior, which is in agreement with the magnetic field for an aligned RH wave that propagates anti-sunward. It is clear that the observed right-hand circular polarization of the wave cannot be attributed to either an inward ion cyclotron wave (in blue) nor an inward whistler wave (not shown but with smaller velocity $v\varphi - V_{\rm SW}$), as this would correspond to a smaller phase velocity and therefore require longer effective length by a factor of 1.5 to 2. The third example on Fig. 8 shows a high density case where the coherence and phase difference are similar than in the previous example but for which the observed velocity is larger than expected, by a factor of ~ 2. It is representative of the points forming the knee of the effective length at $L_{\rm DEBYE} \sim 4$ m in Fig. 4. As can be seen, the high velocity is incompatible with an ICW propagating towards the Sun – and making it compatible would require a very nonphysical effective length. We don't know any wave modes other than whistler with the capacity to explain these wave properties, and we rather tentatively attribute the discrepancy in velocity to other effects: finite plasma beta or some plasma-antenna interactions as the Debye length becomes short.

We also notice that some observed waves (about 7%) have frequencies below the lower hybrid frequency, $f < f_{\rm LH}$. These

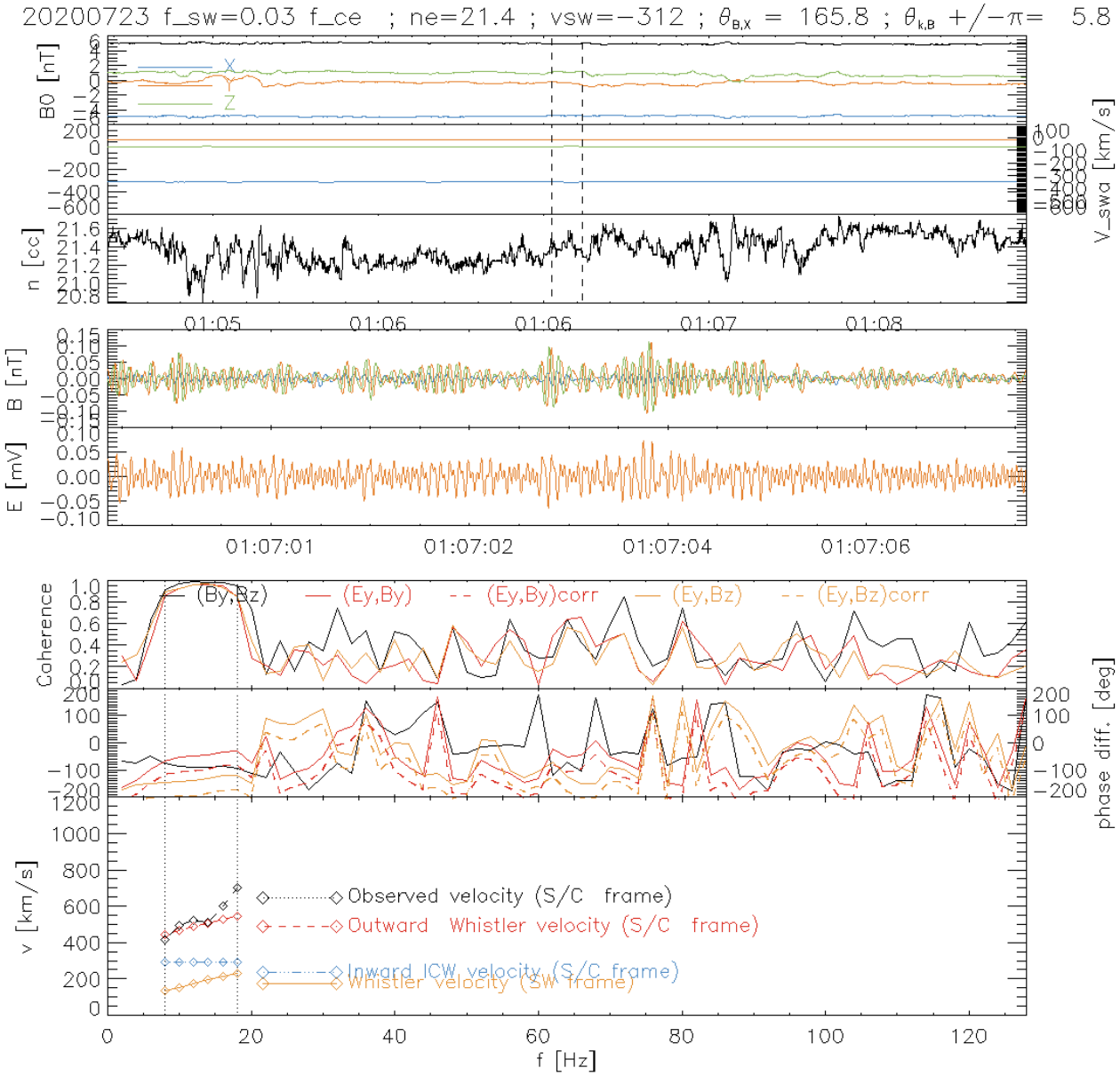

Fig. 6. Wave example 1. The *three first panels* starting from top represents de background magnetic field, the solar wind speed, and the electron density measured by RPW, for a four-minute interval, centered on the snapshot (the vertical dashed lines indicates the snapshot boundary). The *fourth and fifth panels* show the three components and the Y component of the fluctuating magnetic and electric fields respectively: X is in blue, Y in orange, and Z in green. The *three bottom panels* show the spectral coherence, the phase difference (with electric field corrected by −50° in dashed lines), as well as the expected (orange, blue, and red) and measured (black) the wave phase velocity. The dotted vertical lines indicates the frequency range where the computation of the velocity is reliable (coherence greater than 0.8 between B_y and B_z and greater than 0.7 between E_y and B_z).

waves are mostly observed in the regions with high electron density electron densities are higher. However, there are only 22 cases with $f_{sw} < f_{LH}$ for which the frequency in the plasma frame was computed using the observed solar wind speed and not the default value of 350 km s^{-1}. A lower actual velocity would lead to an increase in the frequency. Figure 9 shows a wave event with high density and at low frequency ($0.14 f_{ce}$). In summary, the observed velocity is: 1) too high to be caused by an inward ICW that is propagating at a solar wind speed with a bulk velocity of 288 km s^{-1} and 2) increasing with frequency, which is expected for whistler waves but not of ICW. All these waves with frequency below f_{LH} (but one) have velocities larger than the local Alfvén speed in the solar wind frame, which does not favor an interpretation in terms of ICW. Here, again, we cannot find any wave modes other than whistler to explain these observations.

Let us further note that observing low values of f/f_{ce} for whistler waves is not rare. Jagarlamudi et al. (2020) used Helios data covering about the same range of heliocentric distances as here to find a mean frequency around 0.1 f_{ce} in the spacecraft frame, but also a significant number of waves with frequencies smaller than 0.05 f_{ce}. Similar distribution of f/f_{ce} in the spacecraft frame were found with Parker Solar Probe data by Jagarlamudi et al. (2021). Furthermore, Lacombe et al. (2014) reported examples of whistler waves occurring around 0.03–$0.04 f_{ce}$ as well; Stansby et al. (2016) have compared observed

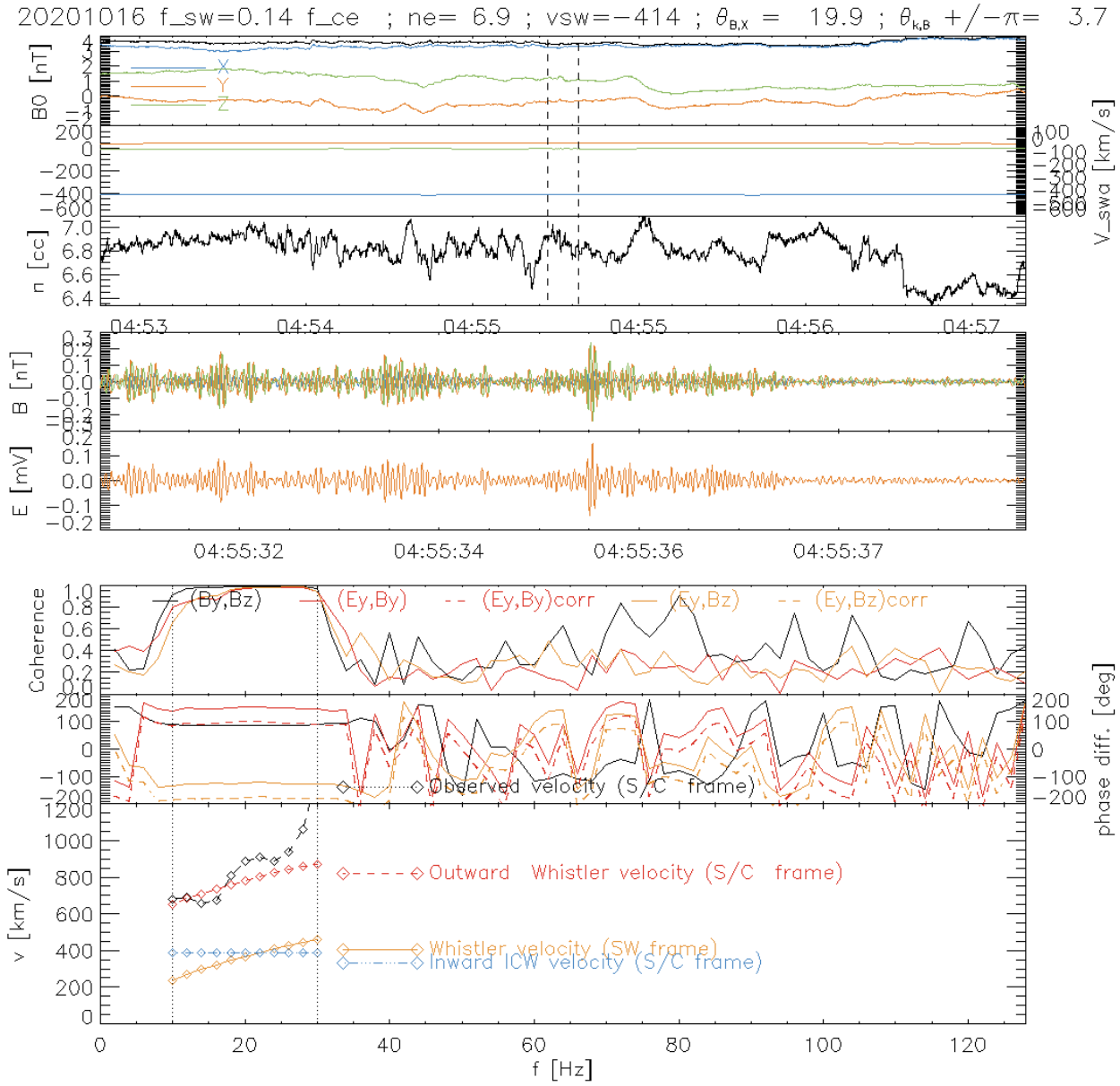

Fig. 7. Wave example 2. The *three first panels* starting from top represents de background magnetic field, the solar wind speed, and the electron density measured by RPW, for a four-minute interval, centered on the snapshot (the vertical dashed lines indicates the snapshot boundary). The *fourth and fifth panels* show the three components and the Y component of the fluctuating magnetic and electric fields respectively: X is in blue, Y in orange, and Z in green. The *three bottom panels* show the spectral coherence, the phase difference (with electric field corrected by −50° in dashed lines), as well as the expected (orange, blue, and red) and measured (black) the wave phase velocity. The dotted vertical lines indicates the frequency range where the computation of the velocity is reliable (coherence greater than 0.8 between B_y and B_z and greater than 0.7 between E_y and B_z).

and theoretical whistler dispersion relation in the solar wind at 1 AU and found whistler waves with frequencies between ~0.03 f_{ce} and 0.2f_{ce}. The values obtained here are therefore consistent with these previous results.

Previous statistical studies of whistler waves below 1 AU were based on Helios and Parker Solar Probe onboard computed spectra only (Jagarlamudi et al. 2020, 2021) and were not able to determine the polarization and velocities of the waves, nor the effect of the Doppler shift. We believe that the detailed analysis presented here strongly suggests, for the first time, that the solar wind between 0.5 and 1 AU is populated with outwardly propagating and quasi-parallel propagating whistler waves.

4. Dependence of the whistler statistical properties properties on the heliocentric distance

We now investigate how the whistler wave parameters vary with the distance. Ideally, we should also take into account the variability of different solar wind parameters, in particular, the solar wind velocity (slow or fast), but also the electron beta and temperature. However, this is impossible for most of the events since the Solar Orbiter / SWA instrument was not observing continuously. For the detected whistler waves with available plasma measurements, during the time interval between July and October 2020, the solar wind velocity was found to be between

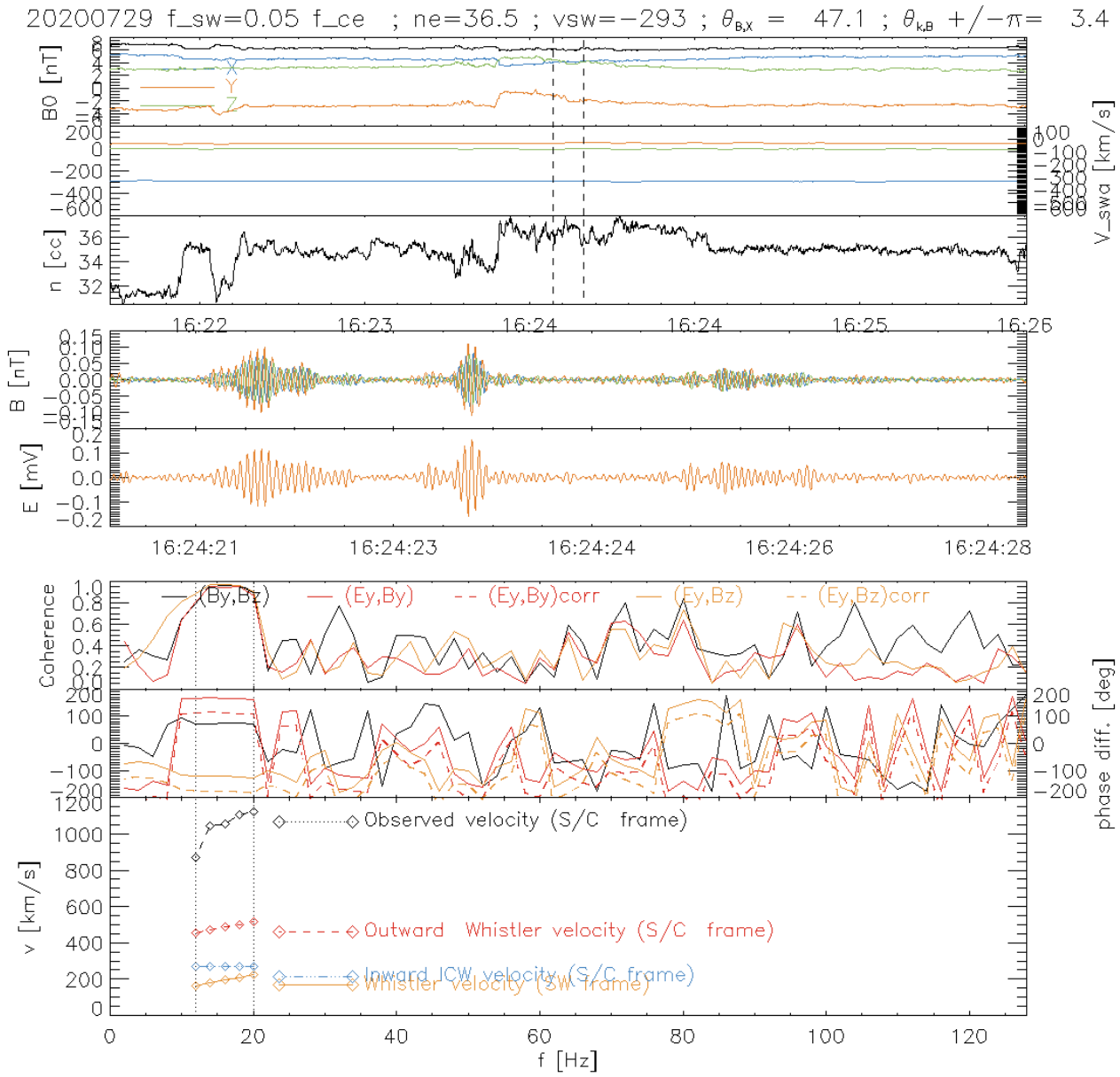

Fig. 8. Wave example 3. The *three first panels* starting from top represents de background magnetic field, the solar wind speed, and the electron density measured by RPW, for a four-minute interval, centered on the snapshot (the vertical dashed lines indicates the snapshot boundary). The *fourth and fifth panels* show the three components and the Y component of the fluctuating magnetic and electric fields respectively: X is in blue, Y in orange, and Z in green. The *three bottom panels* show the spectral coherence, the phase difference (with electric field corrected by −50° in dashed lines), as well as the expected (orange, blue, and red) and measured (black) the wave phase velocity. The dotted vertical lines indicates the frequency range where the computation of the velocity is reliable (coherence greater than 0.8 between B_y and B_z and greater than 0.7 between E_y and B_z).

260 km s^{-1} and 400 km s^{-1} about 88% of the time, and never larger than 530 km s^{-1}. This signifies that the results presented here may be considered to be representative of a slow to intermediate winds, but not of a fast wind. Furthermore, for the first part of the orbit between February and May 2020, the WIND measurements at L1 show that the solar wind velocity were most of the time below 450 km s^{-1} with a few and short incursions above 500 km s^{-1}. The fewer number (see below) of whistler waves observed during this period, when Solar Orbiter was not too far from the Earth, then does not seem to be caused by the presence of a faster wind and the dependence on distance that we observed appears to be real.

4.1. Occurrence rate

We estimated the occurrence rate of whistler waves in two ways. First, we evaluate the ratio of the number of snapshots with at least one whistler wave packet to the total number of observed snapshots, as done in previous studies (Tong et al. 2019a; Jagarlamudi et al. 2020, 2021). This provides us with an upper estimate of the occurrence rate, as it is unlikely that the wave packet stands for the whole duration of the snapshot. Second, we have computed the ratio between the total observed time including whistler waves, as the sum of the duration of each wave packet, and the total time of observations. This provides us with a more precise estimate of their occurrence rate. Both

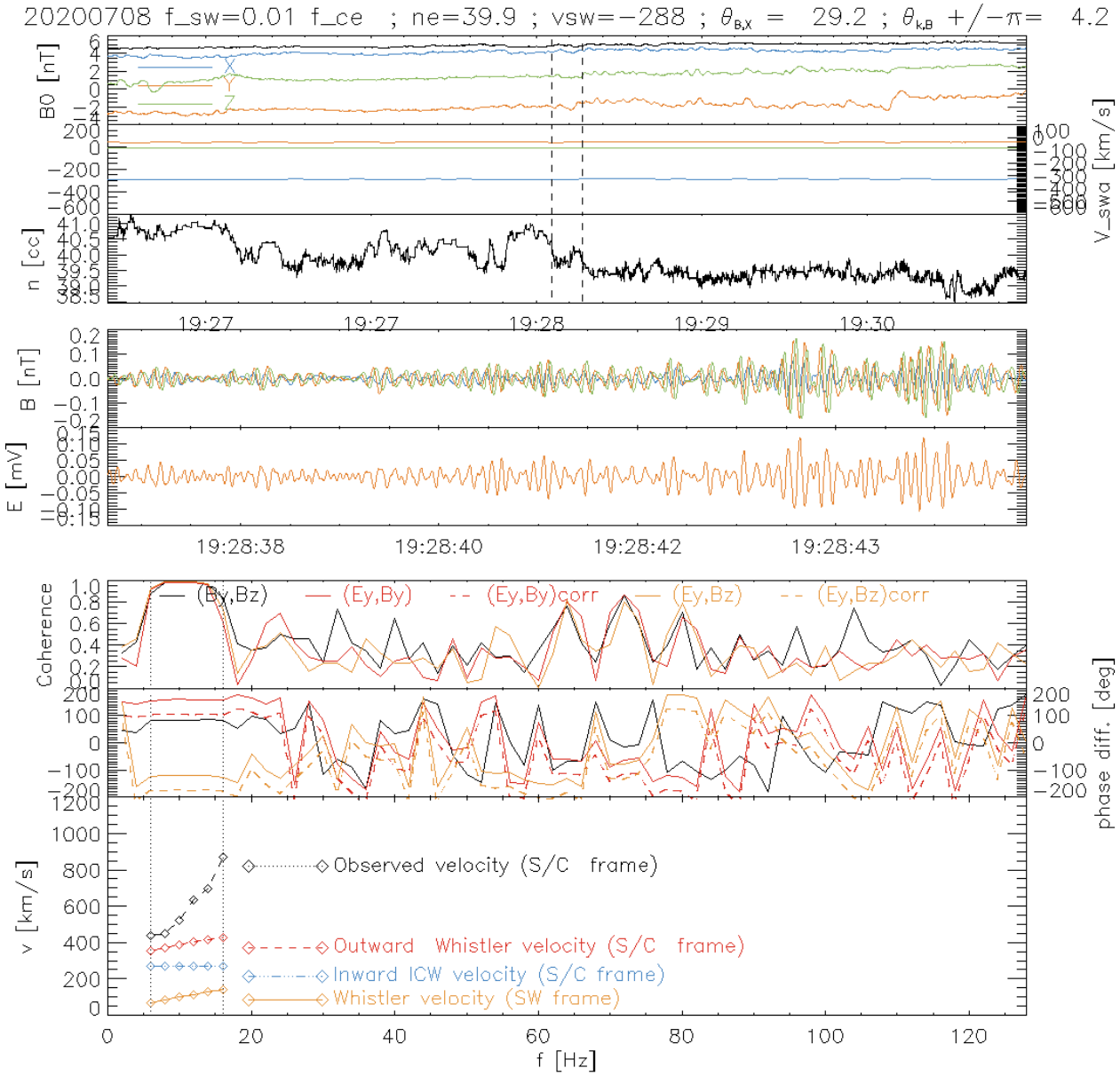

Fig. 9. Wave example 4. The *three first panels* starting from top represents de background magnetic field, the solar wind speed, and the electron density measured by RPW, for a four-minute interval, centered on the snapshot (the vertical dashed lines indicates the snapshot boundary). The *fourth and fifth panels* show the three components and the Y component of the fluctuating magnetic and electric fields respectively: X is in blue, Y in orange, and Z in green. The *three bottom panels* show the spectral coherence, the phase difference (with electric field corrected by −50° in dashed lines), as well as the expected (orange, blue, and red) and measured (black) the wave phase velocity. The dotted vertical lines indicates the frequency range where the computation of the velocity is reliable (coherence greater than 0.8 between B_y and B_z and greater than 0.7 between E_y and B_z).

estimates are however limited by the sensitivity of SCM. Figure 10 shows the occurrence rate, computed over each heliocentric bin and as averaged daily value within the bin (daily ratio averaged over the heliocentric bins). The value at 0.825 AU, which corresponds to observations between 0.8 and 0.85 AU, differs for the two computations. This can be explained by the presence in that bin of the magnetic perturbation that crossed Solar Orbiter on April 13, 2020. On that day, nearly 4000 whistler wave packets have been detected, which explains why the averaged daily ratio is smaller than the ratio computed over the whole interval (19 days). This also evidences that the whistler mode occurrence is not steady and depends on wind conditions, as has been shown by the previous studies.

The value obtained in the bin [0.95–1 AU] with the 8 s average spectrum (snapshot ratio) is close to the ∼1.7% occurrence rate observed at 1 AU by *Artemis* (Tong et al. 2019a). It is however about ten times less than the value obtained by Jagarlamudi et al. (2020) with HELIOS data.

Despite of the statistical fluctuations, we can notice that there is a general trend for whistler waves to occur more often when going from 1 AU to 0.5 AU, varying from an occurrence of ∼2% near the Earth to 5–10% at 0.5 AU (using the snapshot ratio). This is in contradiction with the results of Jagarlamudi et al. (2020), who analyzed HELIOS data and found the occurrence to decrease from ∼15% to ∼3%. These authors had only low-resolution frequency spectra at their disposal and their selection

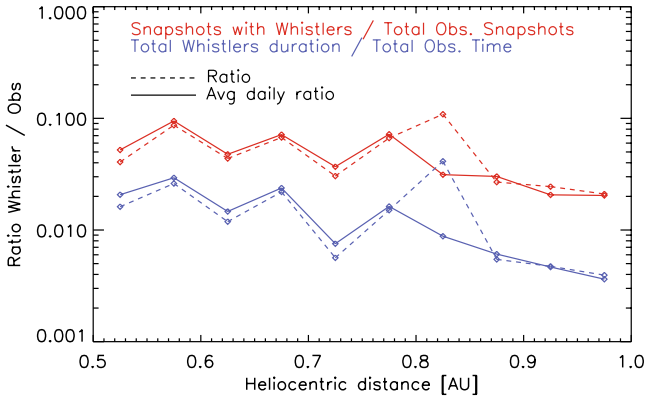

Fig. 10. Variations of whistler occurrence with heliocentric distance. The numbers of snapshots with whistler waves for a given heliocentric distance bin ranges from 237 to 1050.

criteria were therefore based solely on bumps in these spectra. It is therefore possible that Doppler-shifted ion cyclotron waves were counted as whistler waves, although our observations do not support an important presence of ICW at these wavelengths. Another possible explanation resides in the fact that the Helios search coil magnetometer had longer antennas and a sensitivity about five times better at low frequencies than SCM on Solar Orbiter. Jagarlamudi et al. (2020) reported a mean wave amplitude between 0.01 nT and 0.02 nT at 1 AU, and around 0.03 nT–0.04 nT at 0.5 AU. We found the mean amplitude to increase from 0.02 nT to 0.026 nT, corresponding to significantly less intense whistler waves closer to the Sun but similar amplitude at 1 AU (the distribution of the wave amplitudes is shown in the top left panel of Fig. 11). We measured amplitudes down to 10^{-3} nT and 18% of the waves at 1 AU have amplitudes below 0.01 nT. A visual inspection of the distribution does not indicate that we are missing small values either. Therefore, it looks improbable that this difference in sensitivity can explain the difference in the observed occurrence. Another difference between the two studies is that we did not exclude planetary shocks and magnetic clouds (with the noticeable exception of the event on April 13). Jagarlamudi et al. (2020) found the occurrence rate of whistler waves to depend on solar wind velocity, with the largest rates for the slowest wind. However, their slow wind observations also correspond to distance below 0.5 AU. Tong et al. (2019a) did not find any dependence of the occurrence rate on solar wind velocity between 270 km s^{-1} and 630 km s^{-1}. The fewer number of whistler waves at larger distances from the Sun that we observed here, corresponds in part to the spring of 2020 when Solar Orbiter was not too far from the Earth and when WIND observations indicate that slow wind was dominant. Therefore, this does not seem to be related to the presence of a faster wind far from the Sun; unless the wind speed was slower enough at 0.5 AU to compensate for an increasing rate with shorter distance, our finding of more numerous whistler waves at 0.5 AU than at 1 AU appears to be in contradiction with Helios observation.

4.2. Wave properties

In this section, we present the statistical characteristics of the observed whistler waves and their variations with the heliocentric distance. We consider the perturbation that occurred on April 13, 2020 as a sufficiently exceptional event to exclude the waves observed on that day in the following.

The top panels of Fig. 11 show the distribution of the wave's amplitudes at various distances. Whistler waves occurring at closer distance to the Sun have larger amplitudes, which may be interpreted as reflecting a larger amount of free energy available for the generation of waves, in the electron heat flux or in electron anisotropy, for example, at this distance. Although Jagarlamudi et al. (2020) reported no clear trend of the wave amplitude with the heliocentric distance, their figure shows more intense whistler waves closer to the Sun, which agrees with our results. When normalized to the background magnetic field, the wave amplitudes appear to be slightly smaller at 0.5 AU than at larger distance, showing that the wave amplitudes do not scale with the background magnetic field but, rather, depend on other parameters.

The bottom panels of Fig. 11 show the histograms of the frequency and frequency bandwidth for different heliocentric distances. Whistler waves occurring closer to the Sun have lower maximum frequency but larger frequency bandwidth than at 1 AU. This larger frequency bandwidth implies larger energy content in the waves and thus can also be interpreted as reflecting a larger amount of available energy.

Figure 12 shows a tendency for wave packets to be longer at smaller distances from the Sun. This could, however, be an effect attributed to a larger wave amplitude that would make the wave packet remain above the noise level for longer duration of time.

Figure 13 shows, for various heliocentric distances, the normalized histogram of the angle between the **k** vector and the background magnetic field, $\mathbf{B_0}$. As shown previously, most of the waves are quasi-parallel, with angles less than 20°. We can also notice that waves observed near 0.5 AU are more aligned than at 1 AU, a trend that is clear but for which we have no clear explanation for now.

5. Conclusion

In this paper, we report the results of the study of the electromagnetic waves observed by Solar Orbiter in the frequency range between 3 Hz and 128 Hz during its first orbit and covering heliocentric distances between 0.5 AU and 1 AU. Using electric and magnetic fields measurements provided by the RPW instrument, we show that an overwhelming majority of these waves are right-hand circularly polarized in the solar wind frame and correspond to whistler waves. They propagate quasi-parallel to the background magnetic field and anti-sunward. This is consistent with the whistler heat flux instability scenario for the regulation of the heat flux. It is worth noting that this study does not rule out the presence of oblique whistler waves, as these later may be quasi-electrostatic and therefore more difficult to detect with our selection procedures based on magnetic measurements.

Contrary to what was found using HELIOS observations, we observed more whistler waves closer to the Sun, by at least a factor of 2. Solar Orbiter observations during the next orbits will improve the statistics over these distances. Whistler waves are generally intermittent and clumped in short duration (~0.3 s) wave packets. When taking into account their actual duration, their occurrence varies from 0.3% at 1 AU to 1%–2% at 0.5 AU. Whistler wave packets are presumably slightly longer at 0.5 AU than at 1 AU, although this could be an effect of their detectability, as they also exhibit greater wave power at 0.5 AU.

We also found that whistler waves tend to be more field-aligned and to have lower normalized frequency values (f/f_{ce}), larger amplitudes, and larger bandwidths at 0.5 AU than at 1 AU.

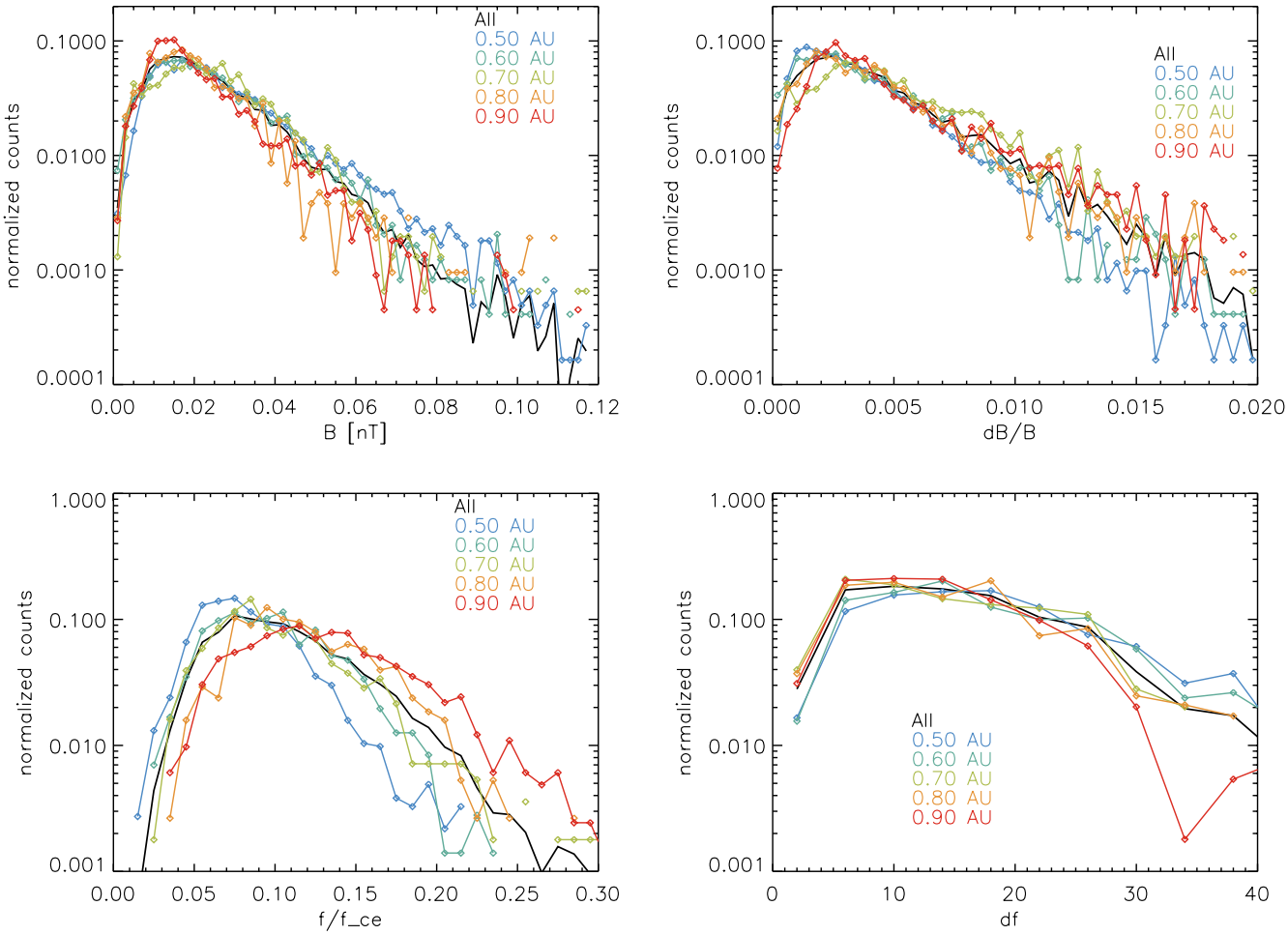

Fig. 11. Normalized histogram for various wave parameters and different heliocentric distances. *Top left*: wave magnetic amplitude *Top right*: wave magnetic amplitude normalized to background field. *Bottom left*: normalized frequency in solar wind frame. *Bottom right:* frequency width.

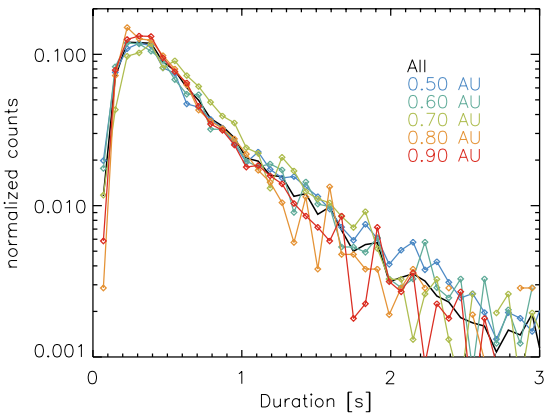

Fig. 12. Distribution of wave packet duration for various heliocentric distances.

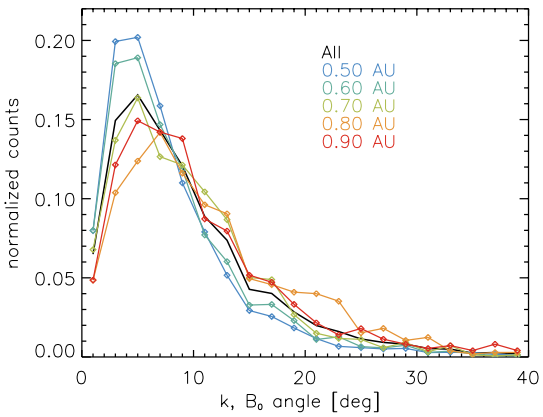

Fig. 13. Distribution of the *k*-vector angles with the background magnetic field.

The larger occurrence, amplitude, and bandwidth clearly indicates that the source of energy that creates whistler waves increases while approaching the Sun from 1 AU to 0.5 AU.

Acknowledgements. Solar Orbiter is a space mission of international collaboration between ESA and NASA, operated by ESA. We thank the Centre National d'Etudes Spatiales (CNES, french space agency) for having funded the Search Coil magnetometer and several subsystems of RPW. D. G. and Y. K. are supported by the Swedish National Space Agency grant 20/136. Solar Orbiter magnetometer operations are funded by the UK Space Agency (grant ST/T001062/1). Tim Horbury is supported by STFC grant ST/S000364/1. Solar Orbiter SWA work at UCL/MSSL is currently funded under STFC grants ST/T001356/1 and ST/S000240/1.

References

Agapitov, O. V., de Wit, T. D., Mozer, F. S., et al. 2020, ApJ, 891, L20
Beinroth, H. J., & Neubauer, F. M. 1981, J. Geophys. Res., 86, 7755

Brent, R. P. 1973, Algorithms for Minimization without Derivatives (Prentice-Hall), 250
Chust, T., Kretzschmar, M., Graham, D. B., et al. 2021, A&A, 656, A17 (SO Cruise Phase SI)
Feldman, W. C., Asbridge, J. R., Bame, S. J., Gary, S. P., & Montgomery, M. D. 1976, J. Geophys. Res. (1896–1977), 81, 2377
Feldman, W. C., Asbridge, J. R., Bame, S. J., Gosling, J. T., & Lemons, D. S. 1978, J. Geophys. Res., 83, 5285
Gary, S. P., Feldman, W. C., Forslund, D. W., & Montgomery, M. D. 1975, Geophys. Res. Lett., 2, 79
Gary, S. P., Scime, E. E., Phillips, J. L., & Feldman, W. C. 1994, J. Geophys. Res., 99, 23391
Halekas, J. S., Whittlesey, P. L., Larson, D. E., et al. 2021, A&A, 650, A15
Horbury, T. S., OBrien, H., Carrasco Blazquez, I., et al. 2020, A&A, 642, A9
Jagarlamudi, V. K., Alexandrova, O., Berčič, L., et al. 2020, ApJ, 897, 118
Jagarlamudi, V. K., Dudok de Wit, T., Froment, C., et al. 2021, A&A, 650, A9
Jannet, G., Dudok de Wit, T., Krasnoselskikh, V., et al. 2021, J. Geophys. Res.: Space Phys., 126, 2020JA028543
Khotyaintsev, Yu. V., Graham, D. B., Vaivads, A., et al. 2021, A&A, 656, A19 (SO Cruise Phase SI)
Lacombe, C., Alexandrova, O., Matteini, L., et al. 2014, ApJ, 796, 5
Maksimovic, M., Zouganelis, I., Chaufray, J. Y., et al. 2005, J. Geophys. Res. (Space Phys.), 110, A09104
Maksimovic, M., Bale, S. D., Chust, T., et al. 2020, A&A, 642, A12
Means, J. D. 1972, J. Geophys. Res. (1896–1977), 77, 5551
Mozer, F. S., Agapitov, O. V., Bale, S. D., et al. 2020, J. Geophys. Res.: Space Phys., 125, 2020JA027980
Owen, C. J., Bruno, R., Livi, S., et al. 2020, A&A, 642, A16
Parail, V. V., & Pogutse, O. P. 1978, Nucl. Fusion, 18, 303
Pilipp, W. G., Miggenrieder, H., Montgomery, M. D., et al. 1987a, J. Geophys. Res., 92, 1075
Pilipp, W. G., Miggenrieder, H., Mühlhaüser, K. H., et al. 1987b, J. Geophys. Res., 92, 1103
Rosenbauer, H., Schwenn, R., Marsch, E., et al. 1977, J. Geophys. Z. Geophys., 42, 561
Santolík, O., Parrot, M., & Lefeuvre, F. 2003, Radio Sci., 38, https://doi.org/10.1029/2000RS002523
Sonnerup, B. U. Ö., & Scheible, M. 1998, ISSI Sci. Rep. Ser., 1, 185
Spitzer, L., & Härm, R. 1953, Phys. Rev., 89, 977
Stansby, D., Horbury, T. S., Chen, C. H. K., & Matteini, L. 2016, ApJ, 829, L16
Steinvall, K., Khotyaintsev, Yu. V., Cozzani, G., et al. 2021, A&A, 656, A9 (SO Cruise Phase SI)
Tong, Y., Vasko, I. Y., Artemyev, A. V., Bale, S. D., & Mozer, F. S. 2019a, ApJ, 878, 41
Tong, Y., Vasko, I. Y., Pulupa, M., et al. 2019b, ApJ, 870, L6
Vasko, I. Y., Krasnoselskikh, V., Tong, Y., et al. 2019, ApJ, 871, L29
Vasko, I. Y., Kuzichev, I. V., Artemyev, A. V., et al. 2020, Phys. Plasmas, 27, 082902